

Moisture Flow as Driving Force behind Drying Shrinkage and Microcracking in Interfacial Transition Zone in Concrete

D. Jankovic*

Gradacacka 37, Sarajevo, Bosnia-Herzegovina

Abstract: In order to determine drying shrinkage in early age cementitious paste and ITZ, prior to a calculation of shrinkage coefficient and further complex coupling, experimental methods at micro-level and numerical methods at meso-level are separately performed as the initial steps. Digital images of a small-size 1-mm thick cement paste specimen with an embedded obstacle as a concrete model are captured at different magnifications and analyzed in drying experiments with Environmental Scanning Electron Microscope (ESEM) and Vic-2D. The drying shrinkage shows the dependence on image magnification, chosen Area of Interest (AOI) and RH variations. Numerical moisture flow/drying simulations by Lattice Gas Automata (LGA) show the difference in a moisture gradient depending on the heterogeneity of the LGA domain (population with smaller and/ or larger solids). Expected higher moisture gradient around larger solids is confirmed in the LGA simulations, which could be an initial sign of gaps/microcracks in real ITZ.

Keywords: Moisture flow, drying shrinkage, microcracks, ITZ, ESEM, LGA.

1. INTRODUCTION

Early age shrinkage microcracks prior to any mechanical loading may be the reason for the collapse of reinforced concrete structures in the later phases of their lives. Microcracks could be induced by time-dependent variations of porous cement paste microstructure as a result of moisture flow (drying) and consequent differential volume changes. As concrete (cement) ages, microcracks may grow into cracks. Their growth may lead to severe failure, since moisture loss and shrinkage become more dependent on the evolving cement microstructure due to external influences. Especially sensitive to microcracks is a highly porous bond zone, between bulk cement paste and aggregate (obstacle), so-called Interfacial Transition Zone (ITZ).

Higher porosity in ITZ develops due to cement bleeding around the aggregates/ obstacles [1] where voids appear to be larger than 5 μ m [2]. A quicker water transport is expected at such 'open' microstructure and in concrete itself, since ITZ may take about 30-50% of the total volume of cement matrix in concrete. Due to its high porosity, the properties of the ITZ vary in comparison to the rest of bulk cement paste (CP). That is why ITZ is considered a concrete-phase with the lowest strength. This emphasizes the importance of moisture flow (drying) investigation of ITZ. Various studies on concrete bond behaviour due to drying and additional loading were conducted in the past

[3-5]. In these drying tests on large concrete specimens (macro-level), cracking was also distinguished as microcracking and bond cracking, which occurred due to the weakening of the bond zone at rather young age, when no load is applied.

The ITZ thickness varies according to various researches. The thickness depends on a concrete characteristics i.e. cement type, w/c ratio, different aggregate qualities, supplementary admixtures and diverse hardening ages, as well as different examination methods. Different researchers found different values of ITZ thickness in a range from 15 μ m [6] to 50-100 μ m [2, 7]. Due to drying, shrinkage deformations (ϵ_{sh}) are related to moisture content (h). L'Hermite [8] described them as directly proportional (1):

$$\Delta\epsilon_{sh} = \alpha_{sh}\Delta h = \alpha_{sh}(E_l - E_L) \quad (1)$$

where E_l is the amount of evaporated water; E_L is the total amount of free water; α_{sh} is the shrinkage coefficient; $\Delta\epsilon_{sh}$ is the difference in the deformations between two consequent drying steps. The shrinkage coefficient (α_{sh}) is expected to vary in ITZ and bulk CP, as a function of variable relative humidity (RH), specimen age, different specimen curing conditions (wet vs. dry), cement quality and other variables.

In order to fulfill structural design needs and produce necessary "cure" for the structure durability, the research on drying shrinkage and possible microcrack occurrence is undertaken in a form of coupling of several scientific branches at two observational levels (micro- and meso-level). The experimental observations of time-dependent cementitious microstructure at micro-level combined

*Address correspondence to this author is Gradacacka 37, Sarajevo, Bosnia-Herzegovina; Tel: +387-33-710-045; E-mail: dj32826@yahoo.com

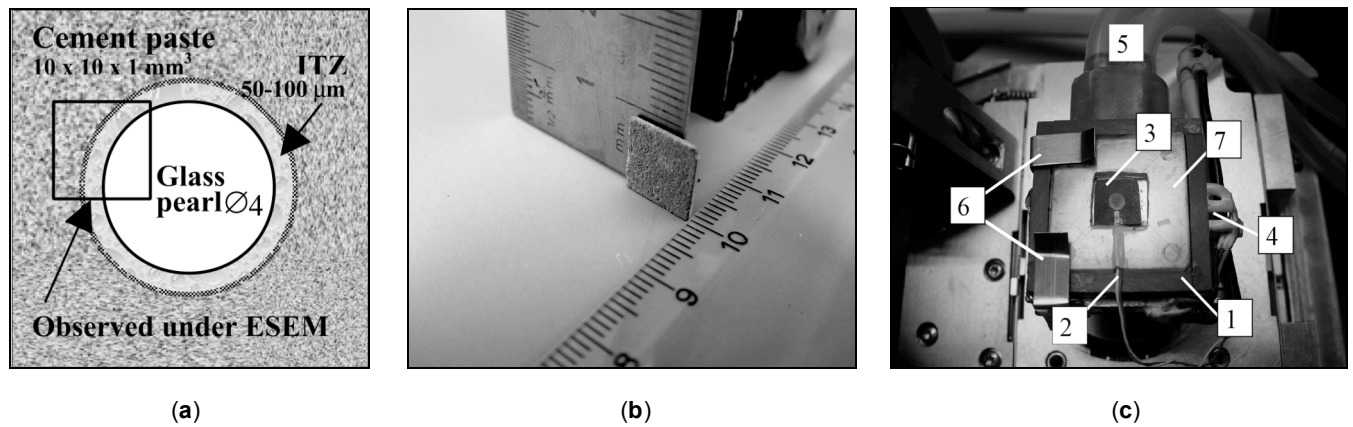


Figure 1: (a) Schematic presentation of cement paste (CP) specimen with glass pearl as aggregate, (b) polished real specimen to size ($10 \times 10 \times 1 \text{ mm}^3$), (c) interior of ESEM XL30 chamber with new cooling house: (1) with inbuilt thermocouple sensors and conductive paste, (2) for temperature measurements on the specimen surface of a specimen (3) and integrated circuits inside the polyvinyl box (4), (5) pipes for liquid circulation, (6) metal clamps, (7) plastic frame around specimen.

with numerical analyses (at meso-level) are considered. As always, one of the research goals is to avoid expensive experiments by performing computer simulations whenever possible.

The next step in the research is to calculate α_{sh} based on shrinkage strains obtained from ESEM shrinkage tests and use it as a link for coupling of two numerical analyzes (Lattice Gas Automata and Lattice Fracture Model) [9, 10]. In that way the change of moisture content during drying from real cement paste specimens would be input in the numerical models. In the previous coupling of these numerical analyzes [9, 10] a constant shrinkage coefficient was initially used from the macro-level experiments on concrete specimens [11].

2. DRYING SHRINKAGE TESTS IN ESEM

In the current analysis, the drying of 32-day old cement paste with an inclusion of a single artificial obstacle (glass pearl, 4-mm, Figure 1) and analysis of drying results are presented. The objective of the previous drying experiments in ESEM, XL30 model [12-14] was to observe drying and shrinkage of a thin cement paste specimen ($10 \times 10 \times 1 \text{ mm}^3$) to recognize the 'real' mechanisms of drying shrinkage in cementitious materials with various characteristics. The observation of real mechanisms is possible if the specimen is thin (1-mm). Such a low thickness should disable development of a moisture gradient in the vertical direction. To avoid microcrack nucleation in the very first days of specimen life, the special preparation technique and drying procedure are developed as described in [12-14] and summarized here.

2.1. Specimen Preparation

Ordinary Portland cement (CEM I, 32.5 R) and demi-water (w/c 0.5) are manually mixed to form cement paste. The specimen is cast in size ($10 \times 10 \times 2 \text{ mm}^3$) in a specially designed mould with the addition of a glass pearl (Figure 1a). Specimen is wet cured in a container with lime-saturated water and kept in the climate chamber at 20°C and 95% RH. Prior to the drying experiments in ESEM, the specimen is manually polished to a thickness of approximately 1-mm (Figure 1b) with a specially designed cylindrical tool [12, 13]. The specimen is fixed at the bottom to ESEM cooling stage by a conductive paste (Figure 1c). The specimen fixing prevents its sliding during drying and improves the temperature control at the bottom of the specimen.

2.2. Drying Procedure in ESEM

Drying and subsequent drying shrinkage strains in specimen are induced by a decrease of relative humidity in ESEM chamber from a fully saturated state at 100% RH to a minimum of 20% RH. The RH is decreased stepwise (by 20%) every time the RH-equilibrium is reached. At each RH step (at 100, 80, 60% etc.) the sharp digital images of high resolution are acquired (Figure 2).

2.3. Magnification and Brightness of Images

The digital image magnification to $50\mu\text{m}$ (referred to as the ESEM magnification of 500x) is selected as a reference magnification for image correlation in all specimens. If microcracks or some extreme displacements are noticed and the conditions during drying tests permitted sharp imaging, magnification is

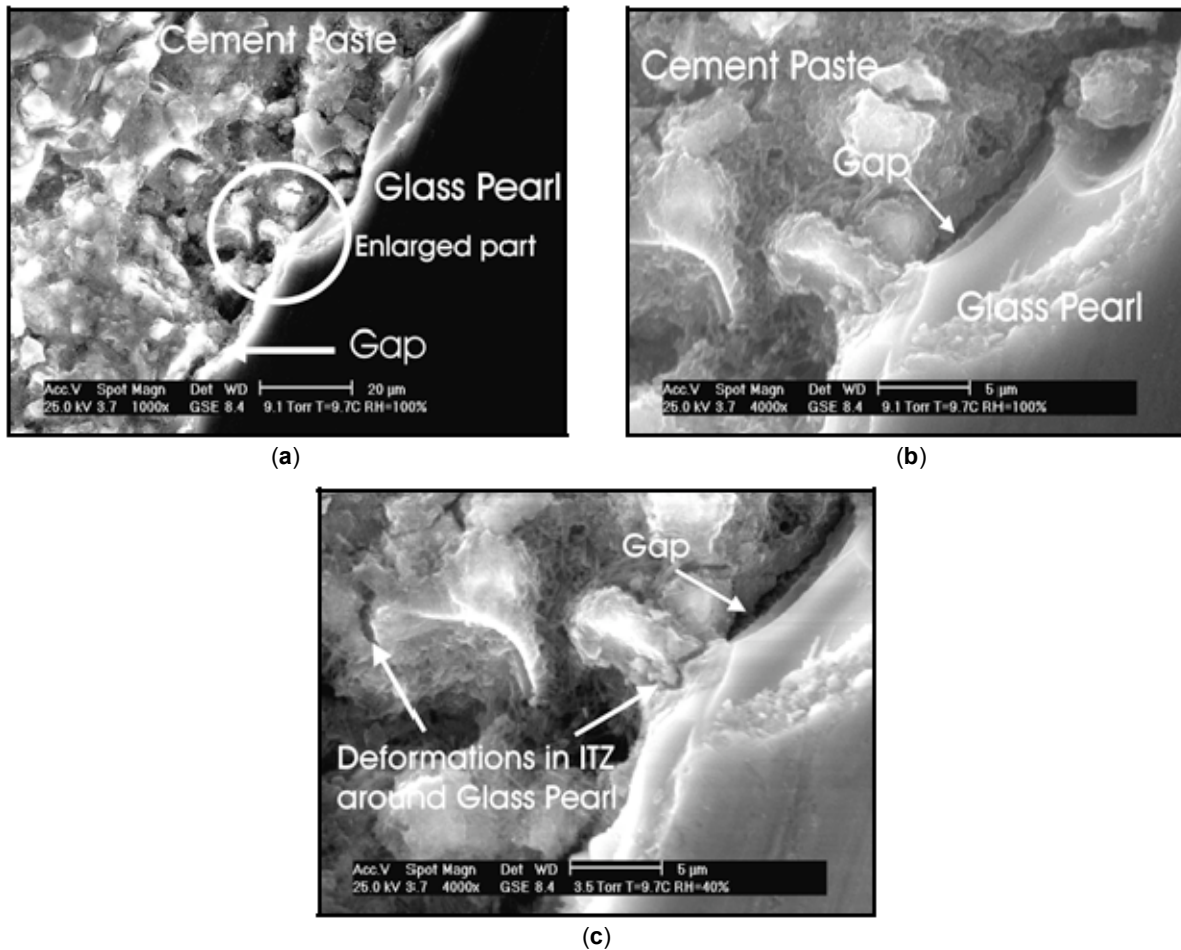


Figure 2: (a) ESEM digital image (1424 x 968 pixels) of ITZ between cement paste specimen and embedded glass pearl at initial saturation stage at 100% RH, magnified to 20 μ m. (b) Enlarged part of image at magnification of (a) 5 μ m, at 100% RH. (c) Drying shrinkage deformations after drying to 40% RH, magnified to 5 μ m.

increased to 20 μ m (Figure 2a), 10, 5 (Figure 2b-c) and 2 μ m (referred to as 1000x, 2000x, 4000x and 8000x respectively). The choice of magnification level relies on the fact that only one spot in a specimen can be chosen to be viewed during entire drying experiment. This is due to the mechanical limitations in ESEM XL30 that occur while trying to move the specimen stage from one observational spot (with the exact coordinates) to another. The brightness and the contrast of images during different drying rates are carefully chosen to maintain the closest possible range in order to avoid large differences and to produce more accurate results.

2.4. Drying Test Results in ITZ

Before the drying at 100% RH started, random, discontinuous gaps of approximately 1- μ m wide and 10- μ m long were visible along the perimeter of a glass pearl in the ITZ (Figure 2a) but only in the surface layer(s) of cement paste. During drying the widening of the gap occurred i.e. de-bonding of cement paste from

the surface of the obstacle (Figures 2b-c) but not the gap deepening. After drying to 20% RH (Figure 3) the gaps appear connected but again only in the surface layers. It seems that cement paste remains closely attached to obstacle in lower cement paste layers even after drying to 20% RH.

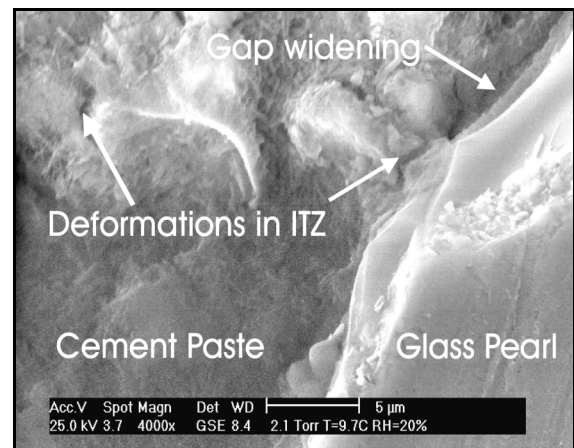


Figure 3: Enlarged circled part of Figure 2a to 5 μ m magnification, at 20% RH.

Speculations could be made about the nature of the gap appearance and its growth during drying. The initial gap that is visible in many specimens could be a result of the missing hydration products between aggregate/ obstacle and paste [2]. Gap could also occur as a surface “peeling” of the cement paste around the obstacle during hydration, due to the obstacle smoothness and low adhesion. Peeling could be an effect of the specimen aging prior to the drying tests. In the first days, possibly up to 7 days, the water film, formed in the mixing process (bleeding) is still present. As the specimen ages (above 28-day), the process of hydration is more or less completed, shrinkage enhances and the gap is clearly noticeable around the obstacle but only on the surface (as in Figures 2b-c, 3). The w/c ratio 0.5 could also influence such drying behaviour. No radial microcracking is observed unlike in younger ITZ (not showed here), where radial microcracking emerged at 20% RH.

3. DIGITAL IMAGE ANALYSIS BY VIC-2D

ESEM images are acquired at different magnifications (50 and 20 μm , Figure 4) in order to compare the

influence of different magnification on shrinkage strains. The calculations of 2-D displacements and subsequent shrinkage strains are based on the cross correlation coefficient and determined using the commercial digital image analysis code Vic-2D.

3.1. Area-Of-Interest (AOI)

The correlation by Vic-2D code is performed in the small-sized Area-Of-Interest (556 x 528 pixels) in both examples, Figure 4. The size of a pixel in (μm) varies with magnification and direction (x or y). For the magnification of 50 μm , the pixel x-size = 0.2 μm and y-size= 0.18 μm . For the magnification of 5 μm , the x-size=0.02 μm , and y-size = 0.018 μm . Hence, the analyzed area is approx. (280 x 180) μm at 50 μm and approx. (28 x 18) μm at 5 μm . The size and shape of AOI are chosen depending on the specimen type (cement paste without or with an obstacle). Here, the AOI is chosen close to the obstacle in ITZ, in the area where no microcracks are seen prior to drying test (Figure 4). Seed point in AOI is typically chosen at the spots where some recognizable features exist. The complete initial guess, which includes displacement and their

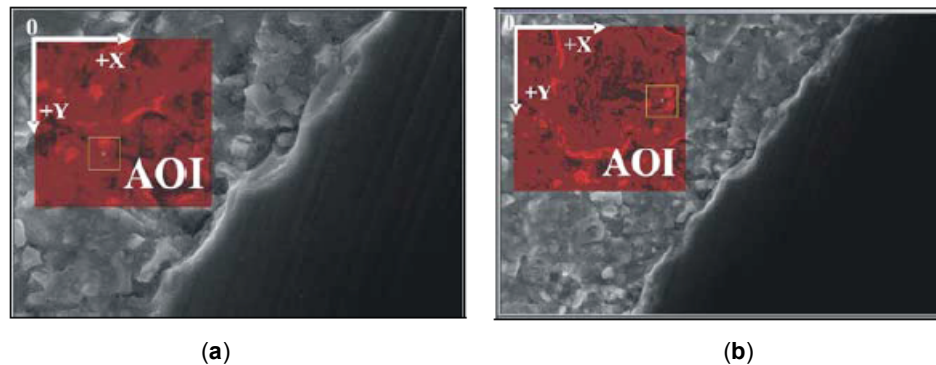


Figure 4: ESEM digital image (1424 x 968 pixels) of ITZ between cement paste and glass pearl. Images are used for the digital analysis of shrinkage strains in AOI (556 x 528 pixels) at (a) at 20 μm and (b) at 50 μm , using Vic-2D code.

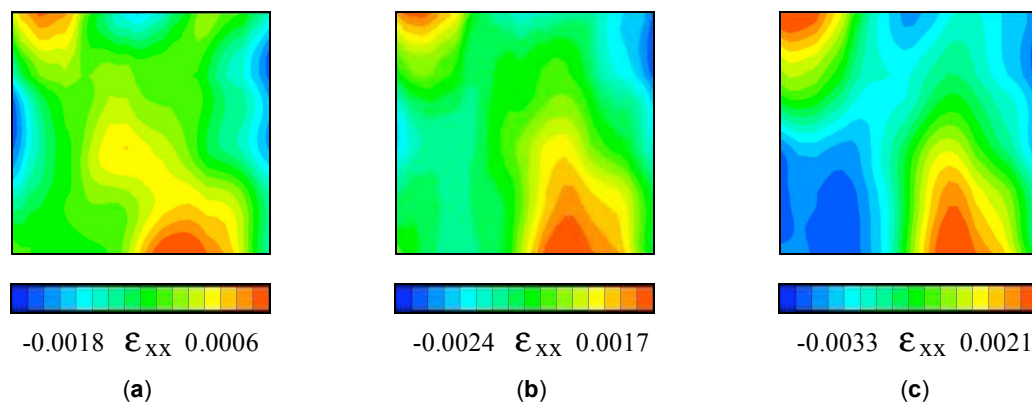


Figure 5: AOI-s at 20 μm with (ϵ_{xx}) distribution (in colours) during drying at (a) 80% (b) 60% and (c) 40% RH, expressed through the strain in every pixel that displaces horizontally to the right (sign “+”) or to the left side (sign “-”) due to the specimen deformations.

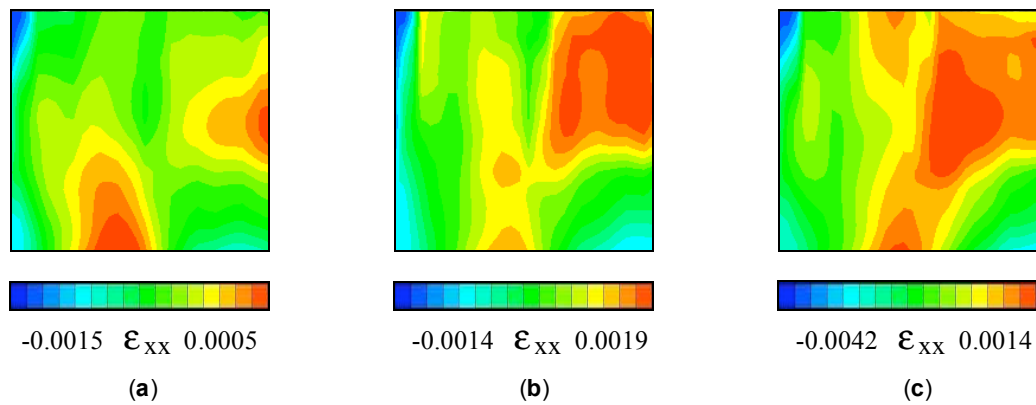


Figure 6: AOI-s at 50μm with (ϵ_{xx}) distribution (in colours) during drying at (a) 80%, (b) 60% and (c) 40% RH, expressed through the strain in every pixel that displaces horizontally to the right (sign “+”) or to the left side (sign “-”) due to the specimen deformations.

derivative approximations is included. The subset-size 100 and step-size 15 are chosen as to obtain good correlation values and the highest shrinkage in all images. As the first step in the final drying shrinkage strain calculations, the displacement of a center of every pixel in the chosen AOI are taken into account and calculated as the average strain value of every pixel in AOI.

3.2. Vic-2D Analysis Results

The characteristic of analyzed ITZ in (Figures 5-6) are coloured ‘layers’. They show non-uniform shrinkage in (x-x) but also in other directions (y-y and x-y), depending on the image magnification and drying level (at 80%, 60% RH etc.). The shrinkage in (x-x) direction is chosen for the current analysis. The colours present different shrinkage strain (ϵ_{xx}) values. Positive ϵ_{xx} sign means layer movement towards the obstacle while negative sign marks a movement from the obstacle. It can be observed that the ϵ_{xx} values at both magni-

fications (50 and 20μm) are of similar order of magnitude. They begin to differ towards drying at 20% RH (Figure 7). All strains at 20μm show an increase (especially ϵ_{xx} , Figure 7a) in comparison to the strains at 50μm (Figure 7b).

Strains increase (Figure 7a) and start to emerge as shrinkage (“-”) and swelling (“+”) at 20% RH. That typically means a nucleation of a microcrack, in this case after drying to 20% RH. Generally speaking, these strain results match the order magnitude of the strains obtained from drying tests by other researchers [15], where different drying techniques are applied.

4. SIMULATION OF MOISTURE FLOW BY LATTICE GAS AUTOMATA

Modeling of moisture flow/ drying is performed using 2-D Lattice Gas Automata (LGA). LGA are often described as an exact numerical solution of the Navier-Stokes equation [16]. The aim of applied numerical analysis is to create a moisture flow through porous

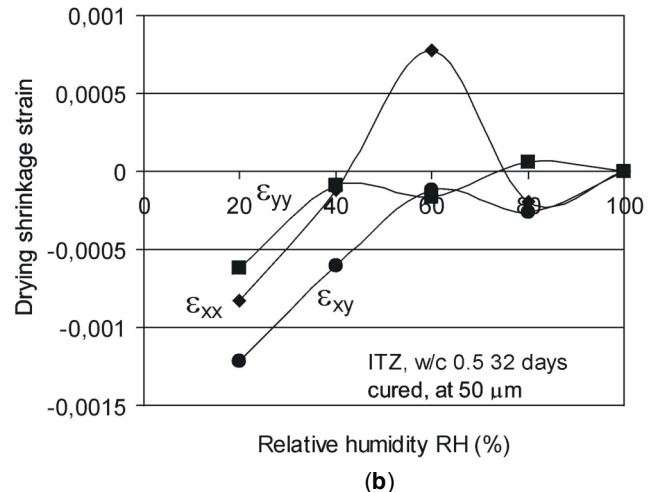
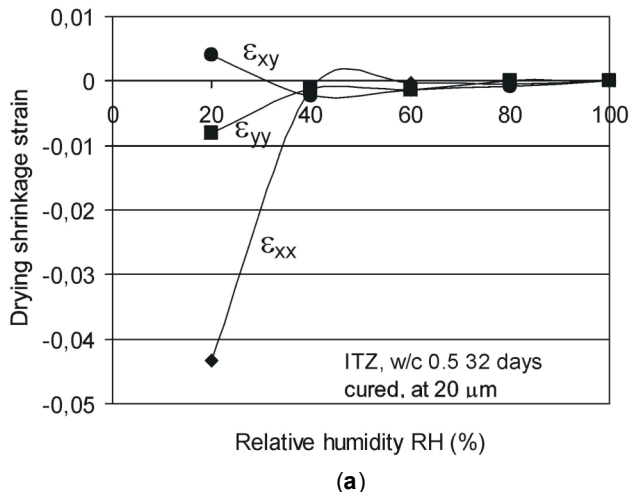


Figure 7: Drying shrinkage strains in ITZ (CEM I 32.5 R, w/c 0.5 with obstacle inclusion), 32-day old. Magnification (a) 20μm and (b) 50μm. Strain data are analyzed in small AOI (556 × 528 pixels).

media (heterogeneous domains) in order to observe the moisture behaviour in the vicinity of the obstacles, earlier defined as the ITZ. That is to see how moisture gradient and speed of drying would vary with the change of LGA characteristics, in order to mimic porous media during drying (curing age, w/c ratio, change in moisture content) as realistically as possible. Former mathematical analysis [17] illustrated that drying shrinkage cracks in concrete depended on the size of the aggregates and their distance. In the current analysis, we introduce different sizes of 'aggregates' (solids) and moisture flow modeling around them to search for LGA parameters that might lead to subsequent microcracking in the numerical coupling to Lattice Fracture Model [10].

4.1. Lattice Gas Automata

Lattice Gas Automata bridge the gap between macroscopic and microscopic phenomena. LGA originate from Statistical Mechanics and Cellular Automata [18]. The main LGA principle is a conservation of mass (number of fluid particles) and linear momentum on the symmetrical system of a hexagonal cell on a triangular lattice (Figure 8a). In order to simulate flow, particles propagate and collide. The similarity between the LGA and the Navier-Stokes (N-S) equation, for incompressible fluid flow is obtained from the Chapman-Enskog expansion [18]. This expansion gives the macroscopic behaviour of fluid by averaging the microscopic (discretized) forms of mass (density) and momentum (2) over the considered area. The density ρ and the linear momentum $\rho\mathbf{u}$, respectively, are defined as follows:

$$\rho = \sum_i N_i, \quad \rho\mathbf{u} = \sum_i N_i \mathbf{c}_i \quad (2)$$

where ρ is a density per node (number of present particles over total possible number of particles); \mathbf{u} is the mean velocity vector; \mathbf{c}_i is the velocity of single particle in any of 6 directions along the lattice spacing l

in time τ , expressed as $\mathbf{c}_i = (\cos(\pi/3) i, \sin(\pi/3) i)$, $i = 0, \dots, 5$. $N_i(x)$ is the average particle population of a cell, expressed as the Fermi-Dirac distribution [18]. N_i can be defined as the probability of particle (i) arriving at node x with velocity \mathbf{c}_i . In the case of unit mass and isotropic velocity distribution, averaging over the lattice area the probability N_i will be $N_i = d$. The probability of a particle leaving the node x will be $N'_i(x)$. The propagation of fluid particles is defined as the conservation of the mean population in the equal probabilities N_i and N'_i as follows:

$$N_i(x + \tau \mathbf{c}_i, t + \tau) = N'_i(x, t) \quad (3)$$

where τ is the time step (chosen as 1). In the steady state, the term t vanishes. The macroscopic equations, obtained through the averaging of the mentioned equations, have close similarity to the Navier-Stokes equation for incompressible fluid flow ($\rho = \text{const}$). In the low velocity limit ($u \ll c$), LGA follow the expression (4):

$$\frac{\partial \mathbf{u}}{\partial t} + g(\rho) \mathbf{u} \nabla \mathbf{u} = -\nabla P + \nu \nabla^2 \mathbf{u} \quad (4)$$

where \mathbf{u} is the velocity vector; P is a pressure; and ν is a kinematic viscosity.

In other words, the LGA is the exact solution of N-S only if the velocity u is smaller than the speed of sound c as mentioned previously ($u \ll c$). The quantity of $g(\rho)$ is not a unity as in the case of Navier-Stokes equation. This is a drawback of Lattice Gas models, which occurs due to the discrete nature of the Lattice Gas. In order to get a close approximation of LGA with low velocity limit incompressible fluid, scaling is necessary. Time, viscosity and pressure are scaled with the factor $g(\rho)$. Detailed derivations can be found in the papers on LGA [16, 18-20].

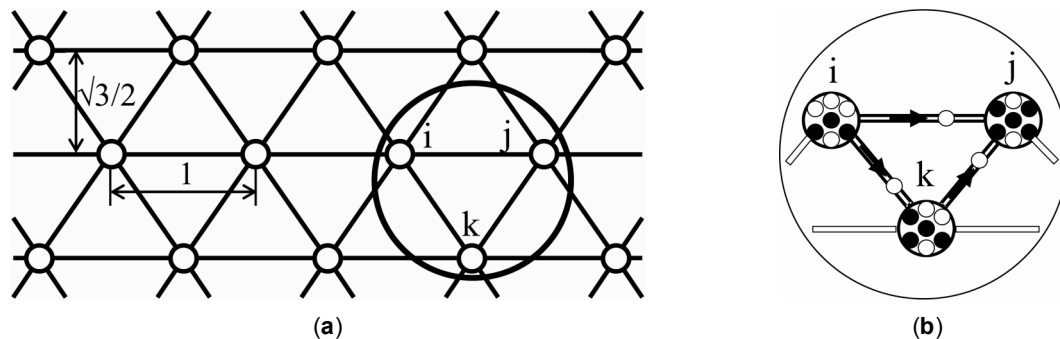


Figure 8: (a) LGA mesh. Lattice in LGA is used as the imaginary track path for propagation and collision of the fluid particles. The distance between any two nodes has a unit value in x-direction and ($\sqrt{3}/2$) in y-direction. (b) FHP model. Enlarged are imaginary paths between (i, j, k) nodes, which allow 'fluid' particles to move from node to node.

4.2. FHP Drying Model

The FHP seven-particle model (Figure 8) is applied in all drying simulations. Maximum seven (fluid) particles exist in every cell (node), which form together a regular, triangular (Bravais) lattice (Figure 8a). One particle out of seven is at rest i.e. having zero velocity, while the remained six 'fluid' particles are able to move in the six directions (Figure 8b).

All fluid particles have unit speed, mass and equal initial density ($d_0 = d$), regardless of the six paths on which they move. Total number of lattice sites in a chosen squared LGA domain is ($X \times Y = 1024 \times 1024$) i.e. $X/Y = 1$. The (1024 x 1024) size was chosen for the better averaging analyses of LGA 'heterogeneous' domains. These domains are populated with smaller/larger solid particles. Solids are coded in a number of 'solid' clusters. The nodes included in the clusters, contain 'solid bit' (8-bit) to differ from other 'fluid' bits. Positions of solid clusters are defined by x-y lattice node coordinates. Solid particles are placed statically on the vertices at predetermined positions, while fluid particles move/ propagate or collide with them in the six directions on the lattice.

4.3. Collision Rules and Boundary Conditions

Collision rules are distinguished as collisions among fluid particles (located in the look-up tables), collisions of fluid with solid particles and collision of fluid particles with solid boundaries. Collision of fluid particles with any solid is given as a ratio r ($r = \text{specular/bounce-back reflection}$), ranging from 0 (bounce-back) to 1 in the specular-reflection. In the given examples, the bounce-back collision rule with the solid wall is applied in all cases. FHP2 collision rule is used from the look-up tables [19]. The FHP2 rule counts 22 collisions, out of 128 possible configurations. Collision rules and number of collisions do not influence the basic macroscopic

equations but only the transport properties such as viscosity. The applied boundary conditions are periodic in the vertical direction, with the wall placed on the left-hand side such that fluid particles that exit cannot re-enter the lattice again. The influence of the number/type of collisions on the drying simulations is taken into account with FHP2 rule.

4.4. Heterogeneous Domain

Domain 1: The heterogeneous (1024 x 1024) domain consists of fluid and solid (20 x 20) lattice sites (Figure 9). Two boundary conditions ($r = 0$ and 1) and FHP2 rule are applied. The size of (20 x 20) solid node-clusters is determined according to the size of real obstacles in the previous NMR analysis. The LGA drying is run till 5000 steps. The idea was to observe how domain dries in a chosen number of LGA steps, but not necessarily to find a final number of steps, which would show a completely dried domain.

The drying results (Figures 9-10) show the moisture gradient decrease due to the presence of solids, but increase of the speed of drying (Figure 10). These results can be compared to the homogeneous domain [21], with the same FHP2 rule, where initially a rather steep moisture gradient occurred. A certain agreement of the numerical simulations could be found with experimental results of drying cement paste specimens in experiments with NMR [21].

The moisture gradient is influenced by the choice of the boundary conditions among fluid and solid particles (bounce-back or specular-reflection). In Domain 1, the moisture gradient (Figure 10a vs. 10b) does not vary significantly when bounce-back or specular-reflection rule is applied. The reason could be the shape and the (1024 x 1024) lattice size (compared to 1000 x 100 lattice-sites in [10]) but also the presence of small solids. Their presence induced noisier results,

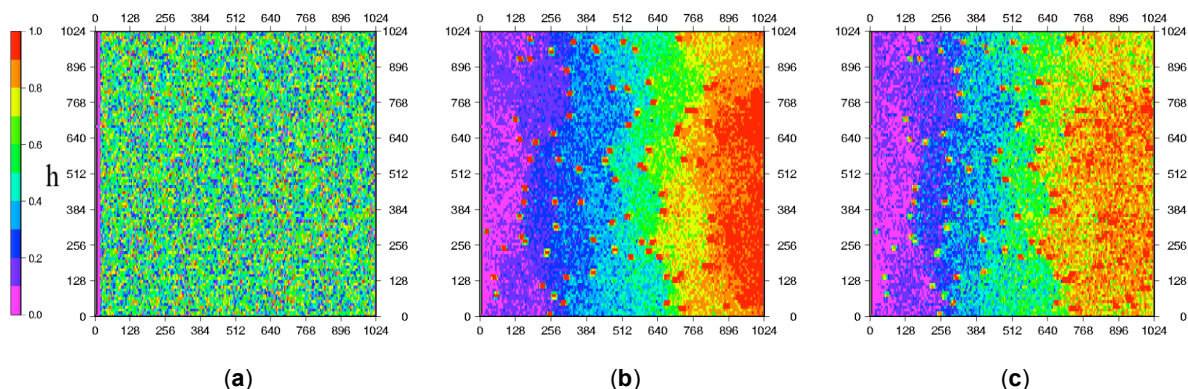


Figure 9: Moisture distribution in Domain 1: drying at (a) 10 and (b) 2000 LGA steps with bounce-back reflection, $r = 0$ and (c) after 2000 steps with the specular-reflection rule $r = 1$. The moisture content is presented in a scale "h".

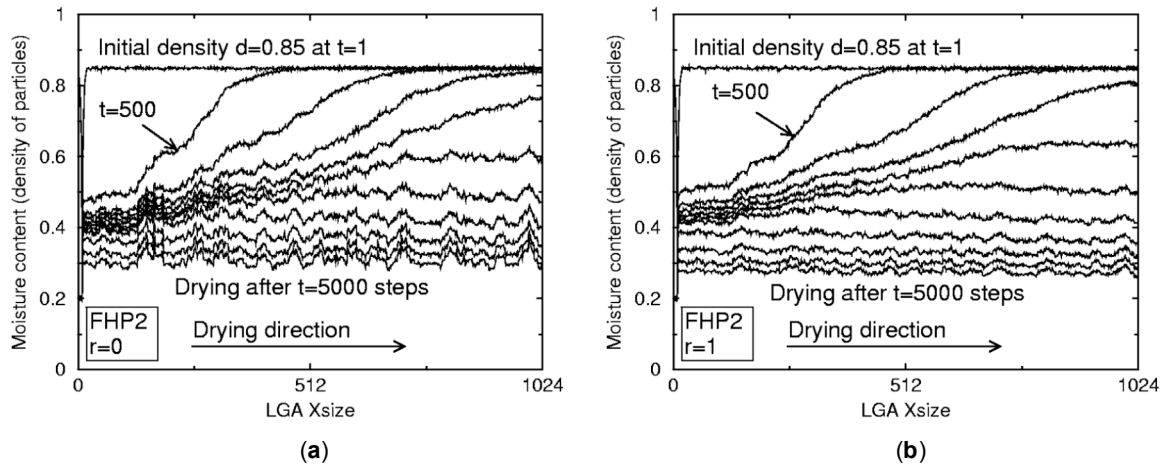


Figure 10: Drying LGA profile in Domain 1. Applied FHP2 collision rule with: (a) bounce-back ($r = 0$) and (b) specular-reflection rule ($r = 1$). Total drying till 5000 LGA steps with averaging in $t = 500$ steps.

especially when the bounce-back reflection is applied (Figure 10a).

Domain 2: Six larger solids (160×160 lattice sites) are generated, combined with smaller, randomly distributed (20×20) solids (Figure 11). The same boundary conditions are considered. The drying is given in (Figures 11-12). A jump in moisture content (Figures 12) is visible in the vicinity of every large obstacle, where 'ITZ' is created as a boundary layer, with a prescribed bounce-back collision rule between fluid and solid particles. This jump could be explained physically and mathematically.

In drying, as a physical phenomenon, significant changes in the moisture gradient are expected in the ITZ (obstacle/ matrix) as it is a highly porous medium and moisture flow occurs with a higher velocity. The density of fluid particles and the velocity should have different values in the matrix (fluid particles) than in the zone between impermeable solids and fluid. The mathematical explanation comes from the Chapman-

Enskog expansion and the Boltzmann equation. It is known that the Chapman-Enskog expansion is used to derive the macroscopic laws when the Boltzmann equation is known. Although the Boltzmann equation is limited to dilute gases so it must be extended for higher collisions (BBGKY hierarchy), we can assume that Boltzmann equation is true for the sake of argument. In the continuous limit, the Boltzmann equation describes the behavior of macroscopic quantities such as the density of fluid particles. It is an equation of function $f(\mathbf{r}, \mathbf{v}, t)$, which expresses how the number of molecules $f(\mathbf{r}, \mathbf{v}, t) d\mathbf{r} d\mathbf{v}$ in the element $(d\mathbf{r} d\mathbf{v})$ of the six dimensional phase space, changes in time t . This function gives the average number of particles in the differential area $d\mathbf{r}$, having a velocity between \mathbf{v} and $d\mathbf{v}$ [22]. The quantity N_i takes the role of the Boltzmann density function f , where the velocities are discrete in six directions (c_i) instead of continuous variable \mathbf{v} . The density of particle (ρ) is defined as an integral of f over the velocity \mathbf{v} , such that density variations (Figures 12) present deviations in velocity.

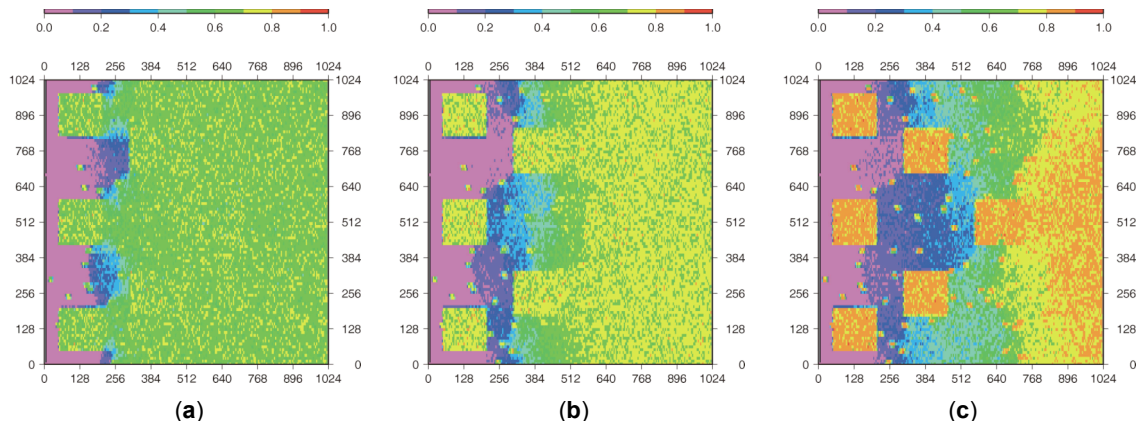


Figure 11: Moisture distribution in Domain 2 with solids (160×160 lattice sites) together with (20×20) at (a) 500, (b) 1000 and (c) 2000 LGA steps. Applied FHP2 collision rule and ($r = 0$). The moisture content is presented in a scale above.

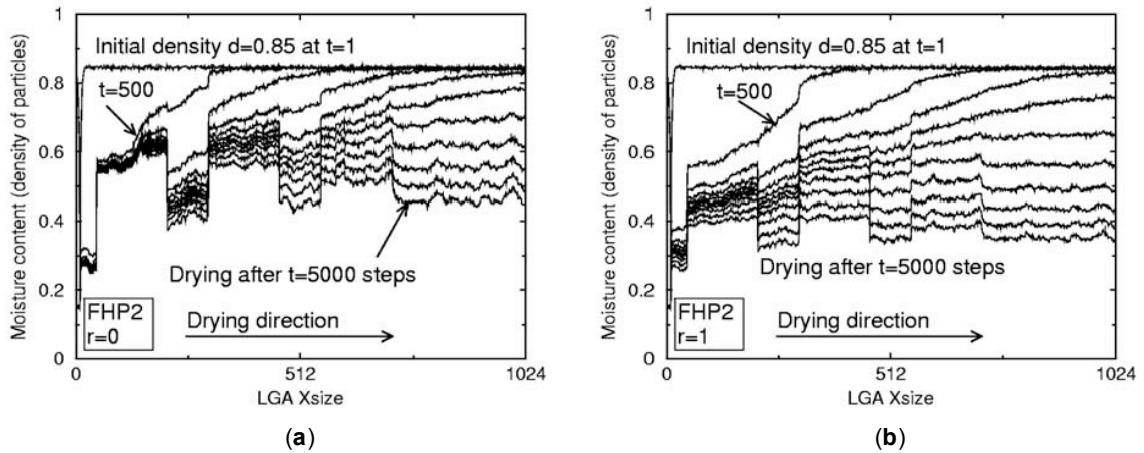


Figure 12: Drying LGA profile in Domain 2 with: (a) bounce-back reflection ($r = 0$) and (b) specular-reflection ($r = 1$). Applied FHP2 rule. Drying to 5000 LGA steps with averaging in 500 steps.

The current LGA analyses run up to few hours. The CPU time depends more on the shape of LGA domain than on its size as well as the presence/absence of solid particles and boundary and collision rules. Presence of solid particles in LGA domain (as in heterogeneous domain) influences quicker drying in comparison to drying of a homogeneous domain [21]. An increase of the lattice size (in comparison to the previous domains) reduces the statistical noise of the results. Complete removal of noise in LGA is difficult to obtain since the LGA is based on Boolean algebra.

5. CONCLUDING REMARKS

The innovative specimen preparation and drying procedure in ESEM at micro-level, enabled observation of processes in ITZ and its deformation without major cracking, so the 'real' shrinkage values could be obtained. However, the drying in ESEM and further image analysis are very complex processes and many parameters should be taken into consideration during analysis. The analysis of ESEM images showed that ITZ is made of several horizontal layers. The surface ITZ layer is detached from imbedded aggregate (glass peal) in a form of a gap, already before drying test started. However, drying to 20% RH showed that lower ITZ layers remained attached to the aggregate.

The digital image analysis and determination of strains by Vic-2D showed dependence on the image magnification in ESEM. The higher the image magnification, the bigger the possibility of microcrack finding due to drying shrinkage. The digital image analysis of strains in small AOI (556 x 528 pixels) at different magnification (50 and 20 μm) showed similar strain values in x-x directions (ϵ_{xx}) until RH was decreased to 20% RH. The ϵ_{xx} at 20% RH at higher magnification (20 μm) appeared over 10-times higher in

comparison to ϵ_{xx} at 20% RH in AOI at lower magnification (50 μm). This implies a microcrack nucleation after drying to 20% RH, which could be only detected at a higher magnification.

Modeling of moisture flow in imaginary ITZ (around the input solids) by means of Lattice Gas Automata at meso-level could be used as an alternative to the complex experimental drying technique later on. The periodical boundary conditions, the number of collisions (i.e. FHP rule) as well as the application of either bounce-back or specular-reflection, have the effect on the moisture gradient and the speed of drying. The speed of drying is also influenced by the number and the size of solids as well as their locations. If the LGA domain is created as homogeneous or populated with less and smaller-sized solids (20 x 20 lattice sites, Domain 1), drying develops slowly and takes more CPU time. The opposite is valid when larger obstacles are imbedded (Domain 2).

The moisture gradient around larger obstacles in the boundary ITZ layer in the LGA domains depends on the application of either bounce-back or specular-reflection with the same collision rule (FHP2). LGA moisture flow simulation with larger obstacles can be used to simulate drying of specimens with lager aggregates, where a higher moisture gradient could be a sign of possible gaps or microcraks. The gradient could also depend on the relationship between the size of specimen and size of aggregate. Speculations could be made regarding large moisture gradients, which could induce cracks on the specimen surface compared to the case when obstacles are placed further away from the drying surface. Crack could emerge by the positioning of larger number of aggregates on a smaller distance from a surface. This appears to be confirmed in the literature [17] but also

by the large moisture gradient around the obstacle as in these LGA examples. When aggregates are located closer to each other, cracks possibly develop due to development of high moisture gradients on small distances in order to prove that more experimental analyses need to be done as well as the extended coupling of LGA to the fracture model (Lattice Fracture Model).

The currently presented work is a preparation for the further coupling analysis. In the future work, shrinkage coefficient should be calculated using drying shrinkage results from ESEM digital images and analysis by Vic-2D method. The coefficient should be used as the input of material parameters in numerical simulations by Lattice Fracture Model, in order to determine when and where microcracks or gaps may appear in a young cement paste and ITZ.

REFERENCES

- [1] Mindess S. Tests to Determine the Mechanical Properties of the Interfacial Zone. Interfacial Transition Zone in Concrete. (ed. J.C. Maso). RILEM Report 11: 47-63. E and FN Spon, London. ISBN 041920010X.
- [2] Struble L. Microstructure and Fracture at the Cement Paste-Aggregate Interface. MRS Proceedings 1987; 114: 11. doi:10.1557/PROC-114-11.
- [3] Hsu TTC, Slate FO, Sturman GM and Winter G. Microcracking of Plain Concrete and the Shape of the Stress-Strain Curve. ACI Journal Proc 1963; 60 (2): 209-224.
- [4] Hsu TTC and Slate FO. Tensile Bond Strength between Aggregate and Cement Paste or Mortar. ACI Journal, Proc 1963; 60 (4): 465-486.
- [5] Slate FO. and Olsefski S. X-Rays for Study of Internal Structure and Microcracking of Concrete. ACI Journal, Proc 1963; 60 (5): 575-588.
- [6] Ollivier JP and Massat M. The Effect of the Transition Zone on Transfer Properties of Concrete, Interfacial Transition Zone in Concrete. (ed. J.C. Maso). RILEM Report 11. 117-131. E and FN Spon, London. ISBN 041920010X.
- [7] Yuan CZ and Odler I. The Interfacial Zone between Marble and Tricalcium Silicate. Cem and Con Res 1987; 17: 784-792. [http://dx.doi.org/10.1016/0008-8846\(87\)90041-X](http://dx.doi.org/10.1016/0008-8846(87)90041-X)
- [8] L'Hermite RG. Volume Changes of Concrete. In Proc 4th Intern Symp on the Chemistry of Cement NBS, Washington DC Paper 1960; 3: 659-702.
- [9] Jankovic D, Kuntz M and Van Mier JGM. Numerical Analysis of Moisture Flow and Concrete Cracking by means of Lattice Type Models. In Proc 4th Intern Conf on Fracture Mechanics of Concrete and Concrete Structures, May-June, 2001. (eds. R. de Borst, J. Mazars, G. Pijaudier-Cabot and J.G.M. van Mier). Cachan, France 2001; 1: 231-238. AA. Balkema Publishers. <http://repository.tudelft.nl/view/ir/uuid:3d361e66-66f9-4f35-b56e-c46f170162d4/>
- [10] Jankovic D and Van Mier JGM. Crack Development in Concrete due to Moisture Flow. HERON 2001; 46 (3): 169-180.
- [11] Martinola G and Wittmann FH. Application of Fracture Mechanics to Optimize Repair Mortar Systems. In Proc 2nd Intern Conf on Fracture Mechanics of Concrete and Concrete Structures. (ed. F.H. Wittmann). Freiburg: 1995; 1481-1492. AEDIFICATIO Publishers, D-79104.
- [12] Jankovic D and Van Mier JGM. Preliminary Investigation of Drying Shrinkage Cement Paste Specimens. In Intern Conf on New Challenges in Mesomechanics, Aalborg University, Denmark, August, 2002. (eds. R. Pyrz, J. Schjodt-Thomsen, J.C. Rauche, T. Thomsen and L.R. Jensen) 2002; 1: 265-271.
- [13] Jankovic D. Nondestructive Determination of Drying Deformations in Cement Paste by means of ESEM and Digital Image Analysis. Optical Micro- and Nanometrology in Microsystems Technology II. (eds. C. Gorecki, A.K. Asundi, W. Osten). Proc. Of SPIE Europe Photonics Europe 7-10 April 2008, Strasbourg, France 2008; 6995: 69950G1-G12. <http://dx.doi.org/10.1117/12.780731>
- [14] Jankovic D. ESEM Drying Tests: Microcracking Initiation in Thin Cement Paste due to Early Age Drying. In 2nd Intern. RILEM Workshop on Concrete Durability and Service Life Planning, ConcreteLife'09. Haifa, Israel 2009; 7-9: 507-514. ISBN 978 2 35158 074 5.
- [15] Pihlajavaara SE. On the Main Features and Methods of Investigation of Drying and Related Phenomena in Concrete Ph D. Thesis University of Helsinki, Finland, Julkaisu 100 Publication Helsinki 1965.
- [16] Frisch U, Hasslacher B and Pomeau Y. Lattice-Gas Automata for the Navier-Stokes Equation. Physical Review Letters 1986; 56 (14): 1505-1508. <http://dx.doi.org/10.1103/PhysRevLett.56.1505>
- [17] Hsu TTC. Mathematical Analysis of Shrinkage Stresses in a Model of Hardened Concrete. ACI Journal Proc 1963; 60 (3): 371-390.
- [18] Wolfram S. Cellular Automaton Fluids 1: Basic Theory. Journal of Statistical Physics 1986; 45: 471-526. <http://dx.doi.org/10.1007/BF01021083>
- [19] Frisch U, d'Humieres D, Hasslacher B, Lallemand P, Pomeau Y and Rivet JP. Lattice Gas Hydrodynamics in Two and Three Dimensions. Complex Systems 1987; 1: 648-707.
- [20] d'Humieres D and Lallemand P. Numerical Simulation of Hydrodynamics with Lattice Gas Automata in Two Dimensions. Complex Systems 1987; 1: 599-632.
- [21] Jankovic D and Van Mier JGM. Drying of Porous Media: Numerical and Experimental Approach. In Computational Modeling of Concrete Structures, Proc Euro-C Conference 2003, eds. N. Bicanic, R. De Borst, H. Mang and G. Meschke, St. Johann im Pongau, Austria: 2003; 453-462. A.A. Balkema Publishers. <http://repository.tudelft.nl/view/ir/uuid:034463b4-919e-4fb8-8633-af1b2821a949/>
- [22] Chopard B and Droz M. Cellular Automata Modeling of Physical Systems. Cambridge University Press 1998. <http://dx.doi.org/10.1017/CBO9780511549755>

Received on 01-06-2015

Accepted on 03-09-2015

Published on 31-12-2015

DOI: <http://dx.doi.org/10.15377/2409-9848.2015.02.02.3>

© 2015 D. Jankovic; Avanti Publishers.

This is an open access article licensed under the terms of the Creative Commons Attribution Non-Commercial License (<http://creativecommons.org/licenses/by-nc/3.0/>) which permits unrestricted, non-commercial use, distribution and reproduction in any medium, provided the work is properly cited.